

1 **Mechanisms for abrupt summertime circumpolar warming in the Southern**  
2 **Ocean**

3 Earle A. Wilson,<sup>a</sup> David B. Bonan,<sup>b</sup> Andrew F. Thompson,<sup>b</sup> Natalie Armstrong,<sup>c</sup> and Stephen  
4 C. Riser<sup>d</sup>

5 <sup>a</sup>*Department of Earth System Science, Stanford University, Stanford, CA, USA*

6 <sup>b</sup>*Environmental Science and Engineering, California Institute of Technology, Pasadena, CA, USA*

7 <sup>c</sup>*Department of Environmental Health and Engineering, Johns Hopkins University, Baltimore,*  
8 *MD, USA*

9 <sup>d</sup>*School of Oceanography, University of Washington, Seattle, WA, USA*

10 *Corresponding author:* Earle A. Wilson, earlew@stanford.edu

11 **ABSTRACT:** In recent years, the Southern Ocean has experienced unprecedented surface warming  
12 and sea ice loss—a stark reversal of sea ice expansion and surface cooling that prevailed over the  
13 preceding decades. In this study, we examine the mechanisms that led to the abrupt circumpolar  
14 surface warming events that occurred in late 2016 and 2019 and assess the role of internal climate  
15 variability. A mixed layer heat budget analysis reveals that the late 2016 and 2019 circumpolar  
16 surface warming events were triggered by a weakening of the circumpolar westerlies, which  
17 decreased northward Ekman transport and accelerated the seasonal shoaling of the mixed layer.  
18 We emphasize the underappreciated effect of the latter mechanism, which played the dominant role  
19 and amplified the warming effect of air-sea heat fluxes during months of peak solar insolation. An  
20 examination of the CESM1 large ensemble demonstrates that these recent circumpolar warming  
21 events are consistent with the internal variability associated with the Southern Annual Mode  
22 (SAM), whereby negative SAM in austral spring favors shallower mixed layers and anomalously  
23 high summertime SST. A key insight from this analysis is that the seasonal phasing of springtime  
24 mixed layer depth shoaling is an important contributor to summertime SST variability in the  
25 Southern Ocean. Thus, future Southern Ocean summertime SST extremes will depend on the  
26 co-evolution of mixed layer depth and surface wind variability.

27 SIGNIFICANCE STATEMENT: This study examines how reductions in the strength of the  
28 circumpolar westerlies can produce abrupt and extreme surface warming across the Southern Ocean.  
29 A key result is that the mixed layer temperature is most sensitive to surface wind perturbations in late  
30 austral spring, when the regional mixed layer depth and solar insolation approach their respective  
31 seasonal minimum and maximum. This heightened surface temperature response to surface wind  
32 variability was realized during the austral spring of 2016 and 2019, when a dramatic weakening of  
33 the circumpolar westerlies triggered unprecedented warming across the Southern Ocean. In both  
34 cases, the anomalously weak circumpolar winds reduced the northward Ekman transport of cool  
35 subpolar waters and caused the mixed layer to shoal more rapidly in the spring, with the latter  
36 mechanism being more dominant. Using results from the Community Earth System Model Version  
37 1 Large Ensemble, we demonstrate that the 2016 and 2019 Southern Ocean warming events are  
38 consistent with the internal variability associated with the Southern Annular Mode (SAM). These  
39 results suggest future Southern Ocean surface warming extremes will depend both on the evolution  
40 of regional mixed layer depths and interannual wind variability.

## 41 **1. Introduction**

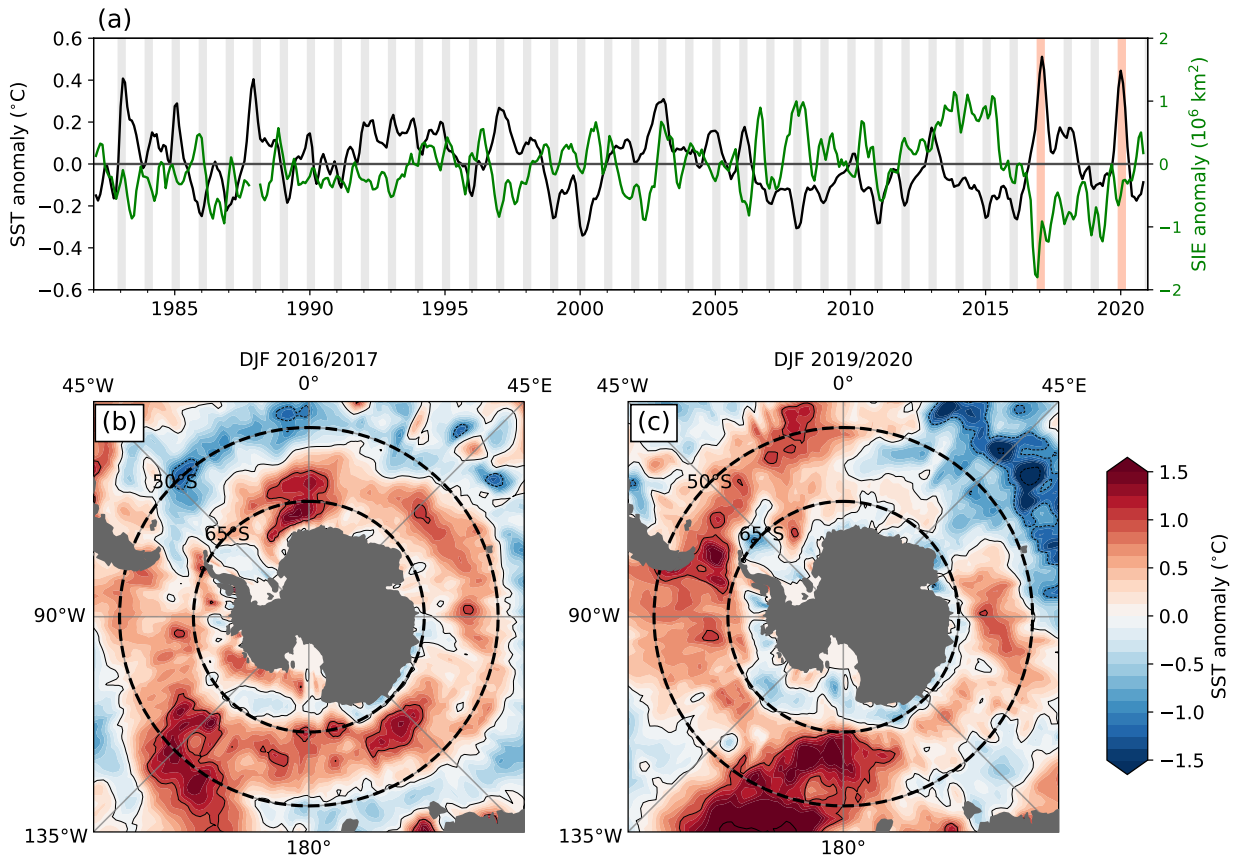
42 The Southern Ocean has experienced exceptional sea ice decline and surface warming in recent  
43 years (Figure 1). During the austral spring of 2016, Antarctic sea ice retreated at an unusually rapid  
44 rate before reaching a record-low extent the following summer (Turner et al. 2017; Parkinson 2019;  
45 Eayrs et al. 2021). This anomalous sea ice decline coincided with widespread surface warming that  
46 extended beyond the Antarctic sea ice zone and culminated in record-high summertime sea surface  
47 temperatures (SSTs) (Stuecker et al. 2017; Meehl et al. 2019, Figure 1a). While Southern Ocean  
48 SSTs returned to normal after a few months, Antarctic sea-ice extent (SIE) remained exceptionally  
49 low over the next three years. In late 2019, the Southern Ocean experienced another abrupt  
50 circumpolar surface warming event of similar magnitude and spatial extent as the anomalous  
51 warming of late 2016, but there was no corresponding decline in Antarctic SIE (Figure 1b).

52 The extent to which these recent warming and sea ice loss anomalies reflect a shift in the Southern  
53 Ocean climate or transient manifestations of internal variability remains unclear. Over the preceding  
54 decades, the Southern Ocean experienced robust sea ice expansion and surface cooling that were  
55 near circumpolar in extent (Yuan and Martinson 2000; Cavalieri et al. 2003; Simmonds 2015). The

56 underlying drivers of these longer timescale trends are uncertain. Possible mechanisms include  
57 the strengthening of the circumpolar westerlies (Fan et al. 2014; Kostov et al. 2017), increases in  
58 surface freshwater fluxes and stratification (Bintanja et al. 2013; Purich et al. 2018; Haumann et al.  
59 2020), atmospheric teleconnections from the tropical Pacific (Meehl et al. 2016; Li et al. 2021;  
60 Chung et al. 2022), and internal climate variability associated with Weddell Sea deep convection  
61 (Zhang et al. 2019). While increased greenhouse-gas emissions will eventually lead to sustained  
62 warming and sea ice loss across the Southern Ocean (Ferreira et al. 2015; Armour et al. 2016;  
63 Kostov et al. 2017), the timescale over which an anthropogenic signal will emerge above the noise  
64 of internal variability is poorly constrained (Doddridge et al. 2019; Rackow et al. 2022).

70 Previous studies suggest that the anomalous decline in Antarctic SIE that began in 2016 was due  
71 to multiple mechanisms operating over various timescales. The initial sea ice loss has been linked  
72 to anomalous variations in the Southern Annular Mode (SAM), El Niño–Southern Oscillation  
73 (ENSO), and Indian Ocean Dipole (IOD), which collectively weakened the circumpolar westerly  
74 jet and facilitated anomalous poleward advection of warm subtropical air into the subpolar region  
75 (Stuecker et al. 2017; Schlosser et al. 2018; Wang et al. 2019; Purich and England 2019). These  
76 mechanisms are distinct from the slower process of enhanced upwelling of warm Circumpolar  
77 Deep Water (CDW) that is expected to drive Southern Ocean sea ice loss and surface warming  
78 over the next century (Bitz and Polvani 2012; Ferreira et al. 2015). However, a gradual build-up of  
79 subsurface heat in the seasonal sea ice zone may have preconditioned some areas of the Southern  
80 Ocean for an unusually rapid springtime retreat of Antarctic sea ice (Meehl et al. 2019; Campbell  
81 et al. 2019).

82 It is likely that the mechanisms responsible for the recent decline in Antarctic sea ice are related  
83 but distinct from those that led to the recent circumpolar surface warming events. Though the 2016  
84 surface warming coincided with a steep loss in Antarctic sea ice, this was not the case in late 2019  
85 (Figure 1a). Furthermore, previous circumpolar surface warming events, such as those that occurred  
86 during the austral spring and summers of 1982/1983 and 1987/1988, were not accompanied by an  
87 appreciable decrease in Antarctic SIE (Figure 1a). As with the late 2016 and 2019 warming events,  
88 other prominent circumpolar warming events extended beyond the seasonal sea ice zone. Though  
89 previous studies have established links between Southern Ocean SST anomalies and the variance of  
90 SAM and ENSO (Sen Gupta and England 2006; Sallée et al. 2010; Ciasto and England 2011; Ding



65 FIG. 1. (a) Temporal evolution of anomalous SST (black) and Antarctic SIE (green) in the Southern Ocean. (b),  
 66 (c) Seasonally averaged maps of anomalous SST during December–February (DJF) of 2016/2017 and 2019/2020.  
 67 In (a), the vertical gray bars highlight austral summer (December–February). Dashed lines in (b) and (c) highlight  
 68 50°S–65°S, the latitudes over which the SST anomalies are spatially averaged in (a). Each time series has been  
 69 smoothed with a 3-month rolling average.

91 et al. 2012; Doddridge and Marshall 2017), there is no clear relationship between the intensity of  
 92 SAM or ENSO phases and the magnitude of Southern Ocean SST anomalies. Thus, the particular  
 93 set of circumstances that facilitated the extraordinary summertime SST anomalies in 2016/2017  
 94 and 2019/2020 remain unclear. Since these surface warming events occur in spring and summer,  
 95 they help set the upper bound on near-surface temperatures that can occur in the Southern Ocean.  
 96 Critically, circumpolar warming events may provide the basis for marine heatwaves (MHWs),  
 97 which are more localized SST extremes that can lead to sharp declines in biodiversity and the  
 98 collapse of ecosystems (Hobday et al. 2016; Frölicher et al. 2018; Holbrook et al. 2019; Smale

99 et al. 2019; Oliver et al. 2021). Therefore, understanding the mechanisms that may lead to surface  
100 warming extremes is an essential step toward characterizing and predicting ecological sustainability  
101 in the Southern Ocean.

102 The primary purpose of this work is to elucidate the large-scale atmospheric and oceanic processes  
103 that give rise to extreme and abrupt circumpolar surface warming across the Southern Ocean. This  
104 work builds on previous analyses that have examined the seasonal evolution of Southern Ocean  
105 mixed layer temperature (MLT) (Dong et al. 2007, 2008; Tamsitt et al. 2016; Pellichero et al.  
106 2017) by focusing on processes that can lead to severe surface warming during summer months.  
107 Likewise, our analysis extends previous work that has explored the Southern Ocean response to  
108 SAM and ENSO (Sen Gupta and England 2006; Sallée et al. 2010; Ciasto and England 2011) by  
109 explicitly examining how the seasonal phasing of these modes of climate variability can produce  
110 extreme summertime SSTs. In doing so, we assess the extent to which recent circumpolar surface  
111 warming anomalies can be explained by internal variability. A key result of this analysis is that  
112 variations in the seasonal phasing of mixed layer depth (MLD) and solar insolation during austral  
113 spring are important contributors to the interannual variability in Southern Ocean summertime  
114 SST.

## 115 **2. Data and Methods**

### 116 *a. Observations and reanalyses*

117 Monthly SST data were obtained from the NOAA Optimum Interpolation (OI) SST V2 product  
118 (Reynolds et al. 2002), while subsurface temperature and salinity variability are assessed from the  
119 Argo-based Roemmich-Gilson climatology (Roemmich and Gilson 2009). Estimates of Antarctic  
120 sea ice concentration (SIC) were retrieved from the NOAA/NSIDC Climate Data Record (CDR) of  
121 SIC (Meier et al. 2013). SIE is defined as the area over which SIC is greater than 15%. Estimates  
122 of surface wind stress, sea level pressure, and air-sea heat fluxes were sourced from the ECMWF  
123 monthly ERA5 global atmospheric reanalysis, which were provided on a 0.25° by 0.25° horizontal  
124 grid (Hersbach et al. 2020). The reanalysis estimates were remapped to a coarser 1° by 1° horizontal  
125 grid using a bi-linear interpolation scheme to be consistent with the RG Argo and the NOAA OI  
126 SST data products.

127 While the SST data and atmospheric reanalysis products are analyzed for 1982–2020, the mixed  
128 layer heat budget analysis is carried out for the 2004–2020 period when subsurface Argo data are  
129 available. The depth of the mixed layer is defined using a density threshold of  $0.03 \text{ kg m}^{-3}$  (de  
130 Boyer Montégut et al. 2004). The SAM index is defined as the zonal-mean sea level pressure  
131 difference between  $65^\circ\text{S}$  and  $40^\circ\text{S}$  (Marshall 2003). ENSO variability is quantified using the  
132 Niño3.4 index, which describes the area-averaged SST anomaly between  $170^\circ\text{W}$ – $120^\circ\text{W}$  and  
133  $5^\circ\text{S}$ – $5^\circ\text{N}$ . The SAM and Niño3.4 indices are normalized by their respective standard deviations.  
134 Anomalies are computed relative to a monthly averaged climatology. For the SST and reanalysis  
135 data, the climatological reference period is 1982–2015, while for the Argo data, the climatological  
136 reference period is 2004–2015.

137 To contextualize recent abrupt circumpolar warming events, observations are compared with  
138 output from the Community Earth System Model Version 1 Large Ensemble (CESM1-LE) (Kay  
139 et al. 2015). The CESM1-LE is a fully coupled,  $1^\circ$  horizontal resolution 40-member initial  
140 condition ensemble, where each ensemble member is subjected to identical historical and RCP8.5  
141 external forcing scenarios. However, each member differs slightly in the initial atmospheric  
142 state, producing a representation of internal variability across ensemble members, in the presence  
143 of forced climate change. We focus on the 1980–2020 period that overlaps with the modern  
144 satellite record. The CESM1-LE uses the Parallel Ocean Program version 2 (POP2), a level-  
145 coordinate ocean general circulation model (Danabasoglu et al. 2012). POP2 employs the K-Profile  
146 Parameterization (KPP) vertical mixing and a mixed layer eddy parameterization to capture the  
147 restratifying effect of submesoscale baroclinic eddies (Fox-Kemper et al. 2008).

#### 148 *b. Southern Ocean mixed layer heat budget*

149 Physical controls on Southern Ocean SST are evaluated using a mixed layer heat budget. In  
150 this study, MLT and SST are assumed to be equivalent. The heat budget is constructed for the  
151 mostly ice-free latitude band of  $50^\circ$ – $65^\circ\text{S}$ , which envelops the core of the circumpolar westerly  
152 jet and much of the Antarctic Circumpolar Current (ACC). This is the latitudinal band over which  
153 SAM induces surface cooling during a positive phase and surface warming during a negative phase  
154 (Sen Gupta and England 2006); further north, between  $30^\circ\text{S}$ – $50^\circ\text{S}$ , the SST response to SAM is  
155 reversed. This analysis focuses on surface temperature variability across the circumpolar band

156 of 50°–65°S since the anomalous warming events of late 2016 and 2019 were most pronounced  
 157 across these latitudes (see Figure 1b-c).

158 As demonstrated by Dong et al. (2007), domain-averaged variations in MLT ( $T_m$ ) across the  
 159 circumpolar channel is primarily governed by heating due to air-sea fluxes, northward Ekman  
 160 transport, and wind-driven entrainment. This balance is given by

$$161 \quad \frac{1}{A_s} \iint \frac{\partial T_m}{\partial t} dA \approx \frac{1}{A_s} \iint \left( \frac{Q_{ao}}{\rho_0 c_w h_m} - v_{Ek} \frac{\partial T_m}{\partial y} - w_{ent} \frac{\Delta T}{h_m} \right) dA, \quad (1)$$

$$162 \quad \frac{1}{A_s} \iint \dot{T}_m dA \approx \frac{1}{A_s} \iint (\dot{T}_{ao} - \dot{T}_{Ek} - \dot{T}_{ent}) dA, \quad (2)$$

$$163 \quad \dot{T}_m \approx \dot{T}_{ao} - \dot{T}_{Ek} - \dot{T}_{ent}, \quad (3)$$

165 where  $Q_{ao}$  is the net air-sea heat flux comprised of the sum of radiative and turbulent heat fluxes,  
 166  $v_{Ek}$  is the meridional Ekman velocity,  $\Delta T$  is the temperature difference between the mixed layer  
 167 and 10 m below the mixed layer,  $c_w$  is the specific heat capacity of seawater,  $h_m$  is the mixed layer  
 168 depth,  $w_{ent} = \dot{h}_m$  is the entrainment rate, and  $A_s$  is the surface area of the circumpolar control  
 169 volume. Here,  $\dot{}$  and  $\bar{}$  symbolize time and spatial averages. The meridional Ekman velocity is  
 170 given by  $v_{Ek} = \tau^x / (\rho_0 f h_m)$ , where  $\tau^x$  is the zonal component of the surface wind stress,  $\rho_0 = 1025$   
 171  $\text{kg m}^{-3}$  is a reference seawater density, and  $f \approx 10^{-4} \text{ s}^{-1}$  is the Coriolis parameter. Following the  
 172 procedure outlined in Dong et al. (2007),  $Q_{ao}$  is modified slightly to account for the fraction of  
 173 shortwave radiation that is transmitted through the base of the mixed layer.

174 Equation (3) is valid when evaluating the heat balance over the entire circumpolar channel.  
 175 Over smaller spatial scales, geostrophic transport and eddy mixing, which are neglected in this  
 176 framework, have leading-order impacts on surface temperature variability (Tamsitt et al. 2016;  
 177 du Plessis et al. 2022; Gao et al. 2022). It is also assumed that meridional eddy fluxes across the  
 178 northern and southern boundaries of the control volume make small contributions to the domain-  
 179 averaged MLT tendency  $\dot{T}_m$  on monthly timescales. Compared to the terms in equation (2), the  
 180 domain-averaged contribution of Ekman pumping on the mixed layer heat budget is negligibly  
 181 small on monthly timescales. Though it is relatively straight-forward to evaluate  $\dot{T}_{ao}$  and  $\dot{T}_{Ek}$   
 182 from Argo data and atmospheric reanalysis,  $T_{ent}$  presents a greater challenge since it is influenced  
 183 by sub-monthly variations in  $h_m$  that are not well-resolved by the current Argo observing array  
 184 (Carranza and Gille 2015). Therefore, the effect of vertical entrainment is estimated from the

185 residual of the other heat budget terms. While other processes, such as submesoscale mixing  
186 and meridional geostrophic advection, and measurement errors may contribute to the residual, we  
187 expect the effect of vertical mixing to be dominant. Vertical entrainment will have a cooling effect  
188 in the summer when the warm mixed layer overlies the cool remnants of the winter mixed layer  
189 and a slight warming effect in the winter when the cold, deep mixed layer is in contact with the  
190 relatively warm circumpolar deep water (Dong et al. 2007).

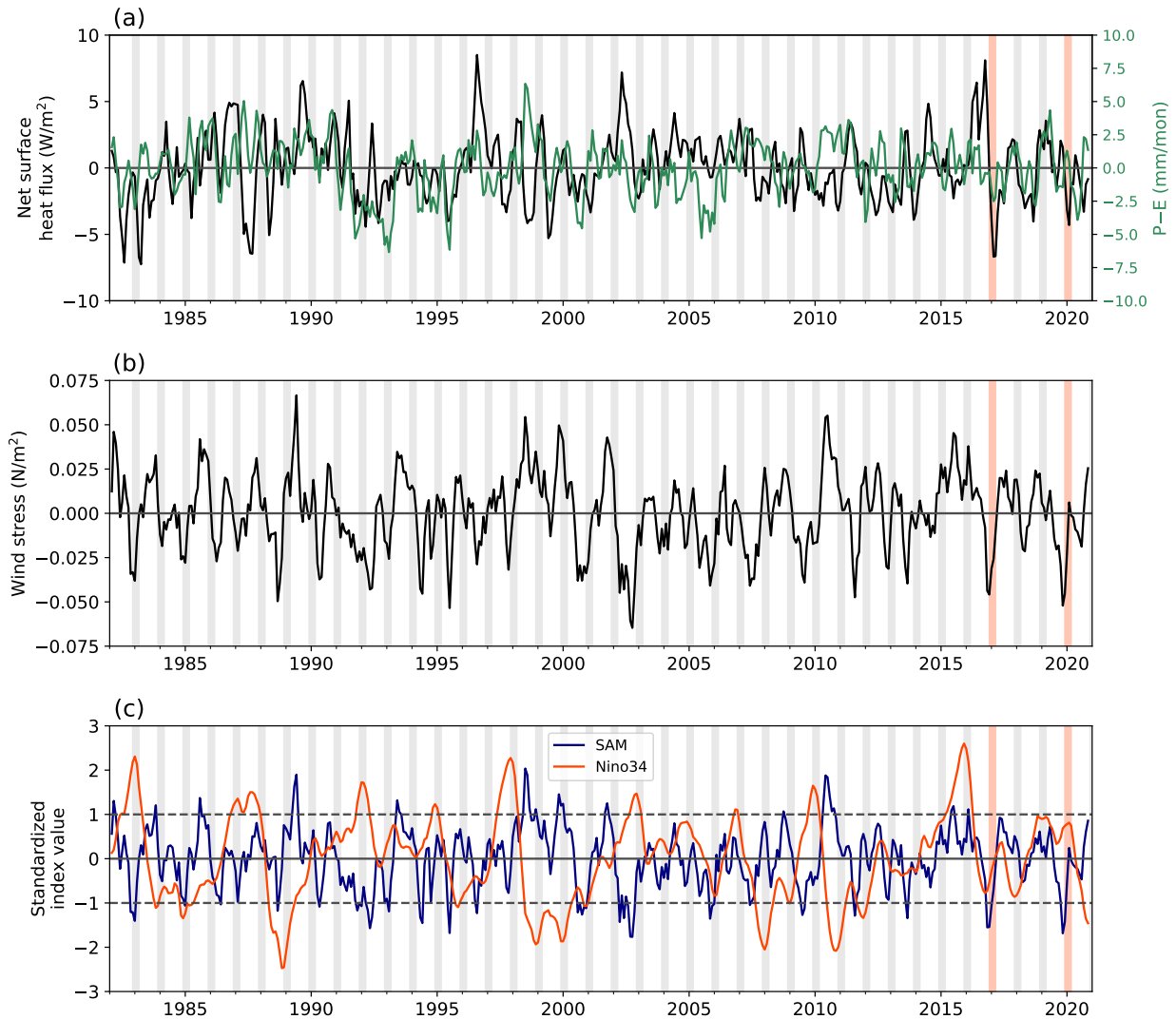
### 196 **3. Results**

#### 197 *a. Environmental conditions during the late 2016 and 2019 Southern Ocean warming events*

204 During the austral spring of 2016 and 2019, the domain-averaged surface buoyancy fluxes across  
205 the Southern Ocean were not consistently different from the climatological mean (Figure 2a).  
206 Though the late 2016 warming event followed unusually warm winter and spring, this was not the  
207 case in 2019. Additionally, the spatial patterns of anomalous air-sea fluxes were not consistent with  
208 the patterns of anomalous warming during both circumpolar warming events (Figure 3). While in  
209 some instances, patterns of anomalously high air-sea heating and mixed layer warming overlapped,  
210 this was often not the case. For example, during November–January of 2019, air-sea heat fluxes  
211 across the southern Atlantic favored anomalous surface cooling while the mixed layer warmed at  
212 an accelerated rate (Figure 3e,f). Thus, the recent circumpolar warming events cannot be directly  
213 attributed to anomalous air-sea heat fluxes.

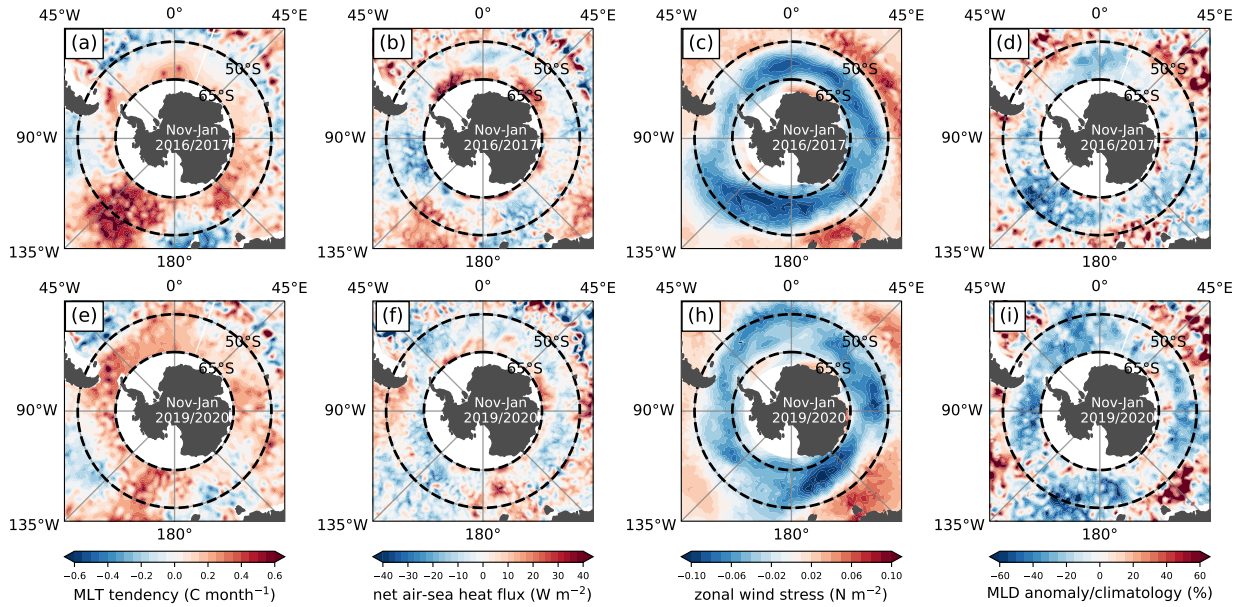
214 On the other hand, circumpolar westerlies were extraordinarily weak in late 2016 and 2019,  
215 with zonally averaged surface wind stress anomalies exceeding  $-0.04 \text{ N m}^{-2}$  (Figure 2b)—a  
216  $\sim 30\%$  reduction relative to the climatological mean. During both warming events, the collapse  
217 of the surface westerlies spanned all longitudes (Figure 3c,h). Concurrently, there was widespread  
218 anomalous MLD shoaling across the Southern Ocean (Figure 3d,i). The anomalous shoaling was  
219 most striking in late 2019 when the MLD across the circumpolar channel was, on average, roughly  
220  $20\%$  shallower than usual. The late 2016 and 2019 anomalous shoaling events did not coincide  
221 with increased surface heat or freshwater fluxes (Figure 2a).

222 Consistent with the strong reduction in circumpolar westerly winds, SAM was in an exceptionally  
223 negative phase during both circumpolar warming events. In both cases, the SAM index was roughly  
224  $1.5$  standard deviations below its annual mean value (Figure 2c). ENSO was in a relatively neutral



191 FIG. 2. (a) Domain-averaged net surface heat flux anomalies (black) and precipitation minus evaporation  
 192 anomalies ( $P-E$ , green) across  $50^{\circ}\text{S}$ – $65^{\circ}\text{S}$ . Positive air-sea heat fluxes signify ocean heat gain. (b) As in (a)  
 193 but showing zonal wind stress anomalies. (c) Temporal evolution of the SAM (blue) and the Nino3.4 indices  
 194 (orange). Vertical gray bars highlight austral summer (December–February). The linear trend has been removed  
 195 from each time series, and temporal variations are smoothed using a 3-month rolling average.

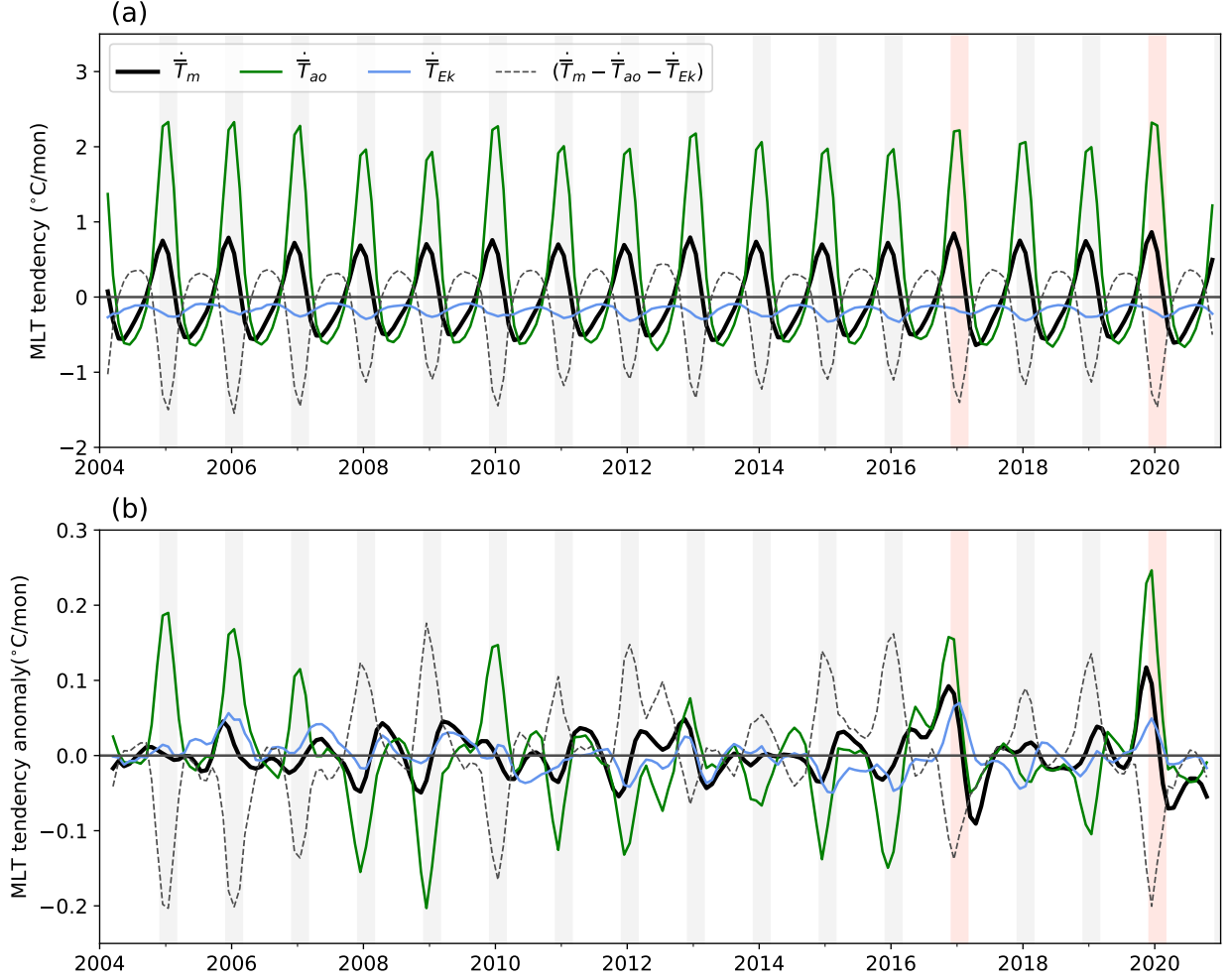
225 state during these periods, tending towards its La Niña and El Niño phases during the austral spring  
 226 of 2016 and 2019, respectively.



198 FIG. 3. Southern Ocean surface conditions during November–January of 2016 (top row) and 2019 (bottom  
 199 row): (a, e) MLT tendency anomalies, (b, f) Net air-sea heat flux anomalies, (c, h) zonal wind stress anomalies,  
 200 and (d, i) MLD anomalies as percentages of the monthly climatological means. Black dashed lines outline the  
 201 circumpolar channel (50°S–65°S) over which the mixed layer heat budget is evaluated. Since the MLD appears  
 202 in the denominator of the heat budget terms (Equation 1), we show the fractional change rather than the absolute  
 203 anomalies.

### 227 *b. Drivers of anomalous mixed layer warming in late 2016 and 2019*

233 Evaluating the circumpolar mixed layer heat budget (Equation 3) reveals that the anomalous  
 234 surface warming in late 2016 and 2019 were primarily caused by heating anomalies associated  
 235 with air-sea heat fluxes  $\dot{T}_{ao}$  and northward Ekman transport  $\dot{T}_{Ek}$  (Figure 4). In late 2016,  $\dot{T}_{Ek}$   
 236 anomalies peaked at roughly  $0.08 \text{ }^\circ\text{C month}^{-1}$ , which was slightly less than the overall mixed layer  
 237 warming of  $0.1 \text{ }^\circ\text{C month}^{-1}$  (Figure 4b). In late 2019, anomalies in  $\dot{T}_{Ek}$  accounted for roughly  
 238 half of the observed mixed layer warming. The decrease in Ekman-driven cooling is consistent  
 239 with the anomalously weak zonal wind stress during these periods (Figure 3c,h). As discussed  
 240 in the preceding section, the increase in  $\dot{T}_{ao}$  cannot be explained by enhanced air-sea heat fluxes  
 241 since these fluxes were not substantially different from the climatology and favored a slight surface  
 242 cooling during the warming events (Figure 2b). This implies that the amplified effect of  $\dot{T}_{ao}$  was  
 243 mainly due to the anomalous shoaling of the mixed layer (Figure 3d,i).



228 FIG. 4. Evolution of the Southern Ocean mixed layer heat budget, described by Equation (3). (a) Monthly  
 229 tendencies in MLT (black) due to air-sea heat fluxes (green) and meridional Ekman transport (blue). The gray  
 230 dashed line represents the residual of the heat budget ( $\dot{\bar{T}}_m - \dot{\bar{T}}_{ao} - \dot{\bar{T}}_{Ek}$ ), which is interpreted as the component  
 231 due to entrainment. (b) As in (a) but after removing the monthly climatology. Gray vertical bars highlight  
 232 December–February.

244 The evolution of the residual of Equation (3) suggests entrainment-driven mixed layer cooling  
 245 was enhanced during late 2016 and 2019 (Figure 4b). In absolute terms, this represents an increase  
 246 in the entrainment-driven cooling that typically occurs in summer months (Figure 4a). The implied  
 247 amplification of  $\dot{\bar{T}}_{ent}$  under weaker surface winds suggests a complex interplay between wind-  
 248 driven mixing, MLD, and the variance of surface winds. Since  $\dot{\bar{T}}_{ent}$  is dependent on MLD and  
 249 the temperature gradient below the mixed layer (Eq. 3), this term does not necessarily scale

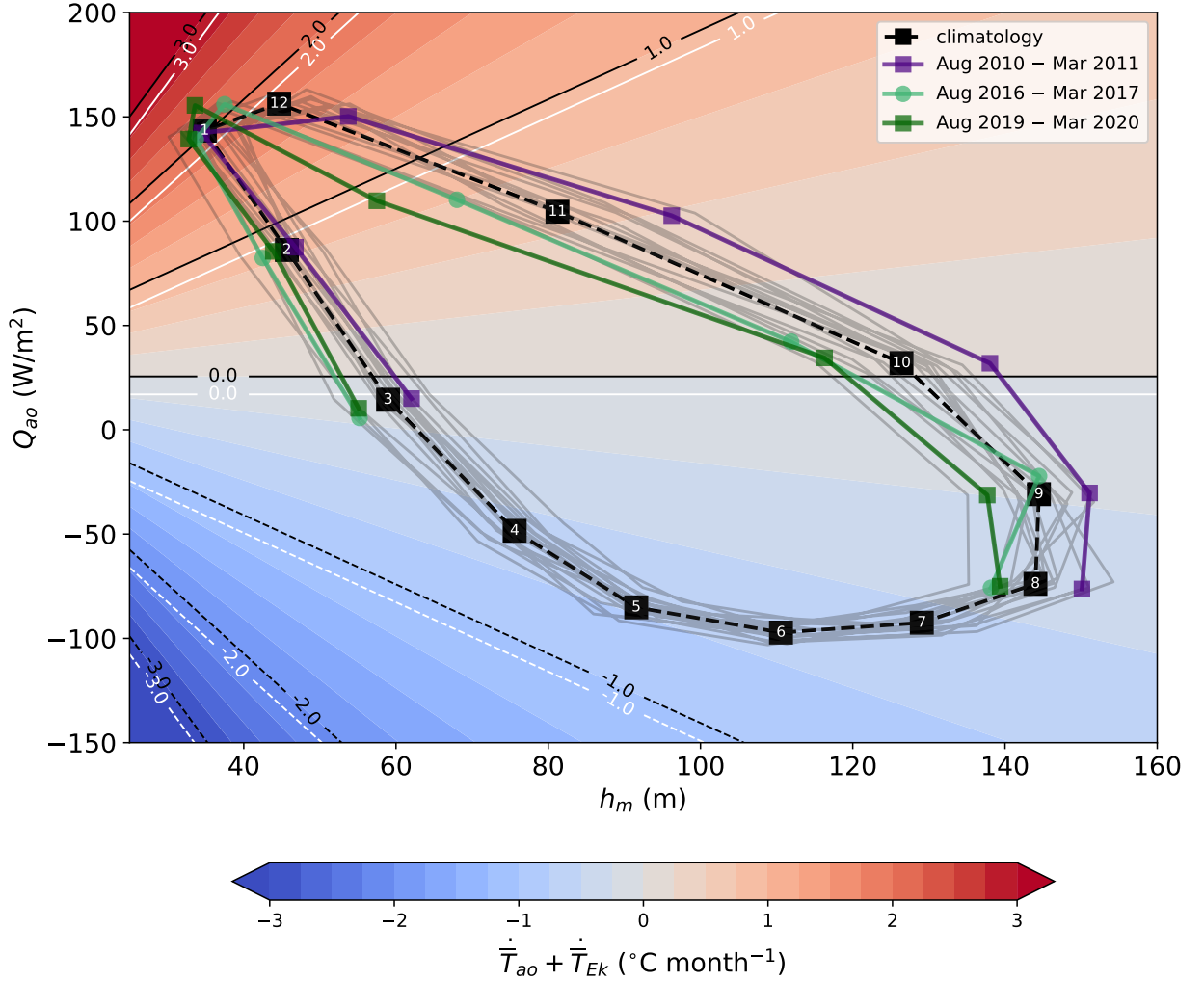
250 with the amplitude of the surface wind stress. Moreover, the temperature of a shallower mixed  
 251 layer will be more sensitive to the mixing generated by episodic storms and strong wind events.  
 252 Nevertheless, without direct estimates of entrainment-driving mixing, the contribution of  $\dot{T}_{ent}$  is  
 253 not well constrained.

262 *c. The seasonal phasing of mixed layer depth and air-sea heat fluxes*

263 The heat budget analysis suggests that the abrupt surface warming events in late 2016 and 2019  
 264 were triggered by a weakening of the circumpolar westerlies and a concurrent shoaling of the  
 265 mixed layer. In the subsequent section, we demonstrate that the latter effect resulted directly  
 266 from the weaker surface winds. Though the surface wind anomalies were relatively large during  
 267 the warming events, the amplitude of these anomalies were not unprecedented (Figure 2b). The  
 268 discrepancies between the relative magnitudes of the surface wind anomalies and concurrent MLT  
 269 anomalies in late 2016 and 2019 suggest other factors were at play.

270 To explore the potential effect of the seasonal phasing of surface wind, MLD, and MLT anomalies,  
 271 we re-examine the seasonal evolution of  $\dot{T}_m$  in the phase-space defined by  $h_m$  and  $Q_{ao}$  (Figure  
 272 5). Since the seasonal variation of  $\tau^x$  is small compared to that of MLD and  $Q_{ao}$ , we focus on  
 273 the sum of the mixed layer warming due to northward Ekman transport and air-sea heat fluxes,  
 274  $\dot{T}_{ao+Ek} \equiv \dot{T}_{ao} + \dot{T}_{Ek}$ , assuming a constant surface wind stress of  $\tau^x = 0.15 \text{ N m}^{-2}$ . During the  
 275 cooling season (March–September),  $\dot{T}_{ao}$  and  $\dot{T}_{Ek}$  combine to cool the relatively deep mixed layer  
 276 at a peak rate of approximately  $0.75 \text{ }^\circ\text{C month}^{-1}$ . During the warming season (October–February),  
 277  $\dot{T}_{ao+Ek}$  provides a surface warming that reaches a maximum of  $\sim 2^\circ\text{C month}^{-1}$  between January and  
 278 February. The seasonal asymmetry of  $\dot{T}_{ao+Ek}$  arises from the nonlinear dependence of  $\dot{T}_{ao}$  on  $h_m$ .  
 279 As  $h_m$  approaches its summertime minimum,  $\dot{T}_{ao+Ek}$  becomes increasingly sensitive to variations  
 280 in  $h_m$  and  $Q_{ao}$ , with  $\dot{T}_m$  being more sensitive to periods of anomalous mixed layer shoaling than  
 281 anomalous deepening. The effect of  $\dot{T}_{Ek}$  may be discerned by the offset in the position of the  
 282  $\dot{T}_{ao+Ek} = 0$  contour in Figure 5; the transect across  $Q_{ao} = 0$  gives the cooling due to northward  
 283 Ekman transport.

284 In the phase-space defined by  $h_m$  and  $Q_{ao}$ , the impact of the extraordinary MLD shoaling in late  
 285 2016 and 2019 is immediately evident. During these anomalous warming periods (green lines in  
 286 Figure 5), the Southern Ocean mixed layer followed a relatively shallow trajectory in the  $Q_{ao}-h_m$



254 FIG. 5. Phase diagram showing the relationship between seasonal variations in mixed layer depth  $h_m$ , air-sea  
 255 heat fluxes  $Q_{ao}$ , and mixed layer temperature tendency due to the sum of air-sea heating  $\dot{\bar{T}}_{ao}$  and Ekman transport  
 256  $\dot{\bar{T}}_{Ek}$  (contours and shading). Gray lines represent seasonal trajectories from 2004–2020, while the dashed black  
 257 line represents the climatological mean. For the latter, the numbering of the black squares signifies the calendar  
 258 month. The purple and green lines highlight trajectories between August–March for 2010/2011, 2016/2017, and  
 259 2019/2020, respectively. For the background shading and black contours, the heating associated with northward  
 260 Ekman transport  $\dot{\bar{T}}_{Ek}$  is computed assuming a typical value of  $\tau^x = 0.15 \text{ N m}^{-2}$ . White contours show  $\dot{\bar{T}}_{ao} + \dot{\bar{T}}_{Ek}$   
 261 for the case where  $\tau^x = 0.1 \text{ N m}^{-2}$ .

267 phase space, which accelerated the springtime warming of the mixed layer. In most years,  $Q_{ao}$   
 268 reaches a maximum amplitude of  $\sim 150 \text{ W m}^{-2}$  in December, one month before  $h_m$  reaches its  
 269 minimum value of  $\sim 40 \text{ m}$ . In late 2016 and 2019, the seasonal  $h_m$  minimum occurred approximately

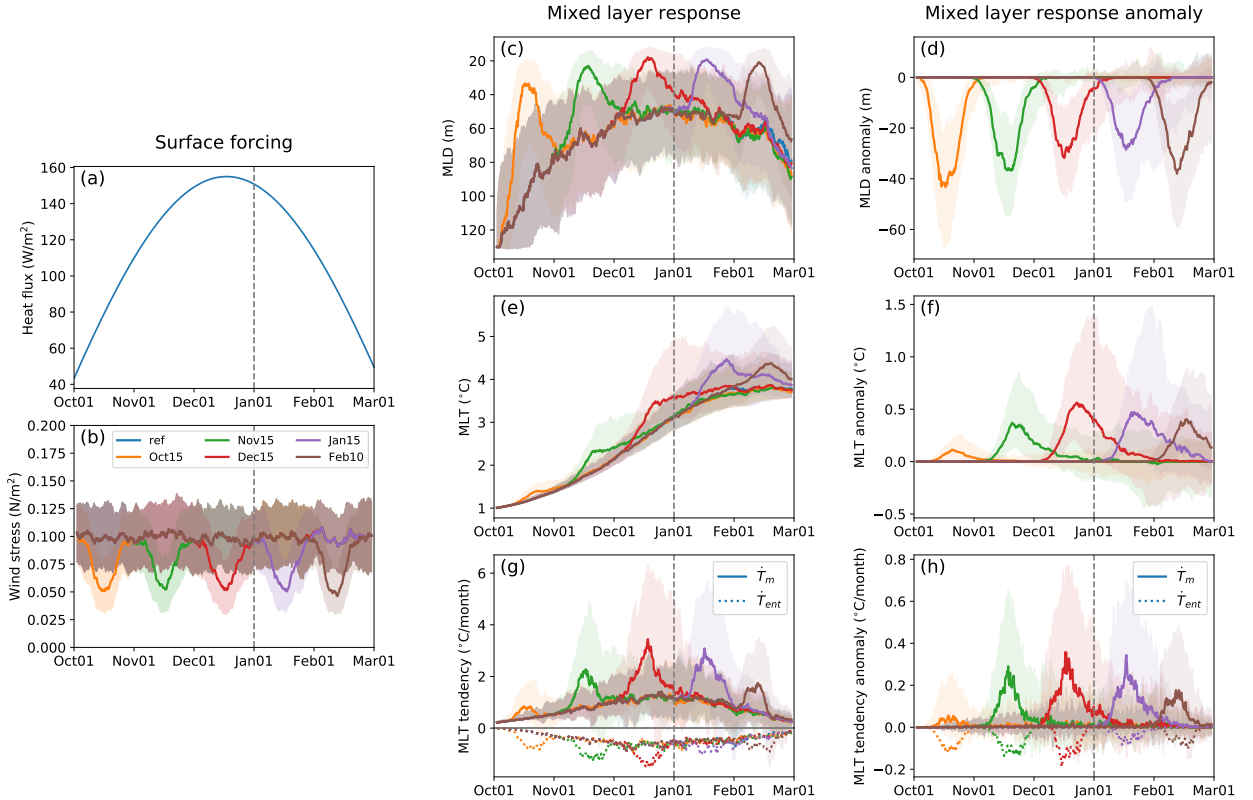
290 one month earlier than usual, coinciding with maximal air-sea heat fluxes. This shoaling-induced  
291 mixed layer warming anomaly was most apparent in November of 2019 when  $h_m$  was 20–30 m  
292 shallower than the climatological mean—a record low for the Argo period. The enhanced mixed  
293 layer warming due to  $\dot{T}_{ao}$  is augmented by a reduction in the cooling provided by  $\dot{T}_{Ek}$ , which  
294 equates to a downward translation of the  $\dot{T}_{ao+Ek}$  pattern in Figure 5. The accelerated mixed layer  
295 warming of late 2016 and 2019, which occurred during strong negative SAM events, is contrasted  
296 with the more gradual warming that occurred in late 2010 (purple line in Figure 5), a period  
297 characterized by positive SAM conditions (Figure 2b,c). In the latter scenario, the anomalously  
298 deep Southern Ocean mixed layer warmed at a relatively slow rate, leading to anomalously cool  
299 summertime surface temperatures (Figure 1a).

309 *d. Sensitivity of mixed layer warming to the timing of surface wind anomalies*

310 The preceding analyses suggest that anomalous mixed layer shoaling and warming during the  
311 austral spring of 2016 and 2019 were initiated by a weakening of the circumpolar westerlies.  
312 To quantify the springtime sensitivity of MLD and MLT to surface wind variability, a set of  
313 idealized simulations were conducted using a one-dimensional ocean mixing model (Appendix  
314 A1). The Kraus-Turner mixed layer model was forced with idealized surface fluxes of buoyancy  
315 and momentum that mimic observations across 50°S–65°S during October and February (late  
316 spring through summer). For the wind stress forcing, we employ synthetic surface winds that are  
317 generated from a red-noise spectrum and have a time-mean magnitude of 0.1 N m<sup>-2</sup>. For a single  
318 experiment, we conducted 200 simulations, each with a unique surface wind forcing.

319 For the reference case, the mixed layer gradually shoals and warms between October and February,  
320 reaching a minimum depth of roughly 50 m and a maximum temperature of approximately 4°C,  
321 which are consistent with observations (Figure 6). In the perturbation experiments, a Gaussian  
322 kernel is used to reduce the time-mean wind stress magnitude by a maximum value of 50% over  
323 various 10-day windows. The time-mean wind strength is reduced during the perturbation period  
324 without modifying the temporal variance.

325 Reducing the strength of the winds increases the rate at which the mixed layer shoals and warms.  
326 The amplitude of the MLD shoaling is not sensitive to the timing of the wind anomaly, with the  
327 median response ranging between 30–40 m. In contrast, the MLT response varies substantially



300 FIG. 6. Results from the idealized 1D mixing experiments. (a) The prescribed surface heat fluxes used in  
 301 all experiments. (b) The synthetically generated surface wind stress used in the reference and perturbation  
 302 experiments, where for the latter set a Gaussian filter was used to dampen the winds by a maximum of 50%  
 303 over five different periods. Middle column shows the MLD (c), MLT (e) and MLT tendency (g) responses.  
 304 The right column (d, f, h) shows the mixed layer response anomalies relative to the reference case with no wind  
 305 perturbation. Each experiment consists of 200 ensemble members forced by a unique wind time series constructed  
 306 from a red noise spectrum. The shading represents the interquartile range, and solid lines represent the median  
 307 response. In (g, h), dotted lines represent mixed layer temperature tendency associated with entrainment  $\dot{T}_{ent}$ .  
 308 The interquartile range for  $\dot{T}_{ent}$  is omitted for clarity. See Appendix A1 for further details.

328 with the timing of the wind perturbation. The median MLT anomaly ranges from 0.1 °C when the  
 329 wind perturbation is applied in mid-October to 0.5 °C when the winds are reduced by an equivalent  
 330 amount in mid-December. The latter warming anomaly occurs when the MLD and surface heat  
 331 fluxes are at their respective minimum and maximum.

332 In the perturbation experiments, weaker winds lead to an increase in entrainment-driven mixed  
 333 layer cooling  $\dot{T}_{ent}$ , which is consistent with what is inferred from observations in late 2016 and

334 2019 (Figure 4). However, the simulated response of  $\dot{T}_{ent}$  is sensitive to the temporal variance of  
335 the surface winds. In experiments where the temporal variance is reduced in a similar manner as  
336 the temporal mean, the change in  $\dot{T}_{ent}$  is negligible (not shown). These results indicate that wind-  
337 driven entrainment is strongly controlled by the temporal variance of the wind stress amplitude,  
338 with high-wind extremes having a disproportionate impact on entrainment.

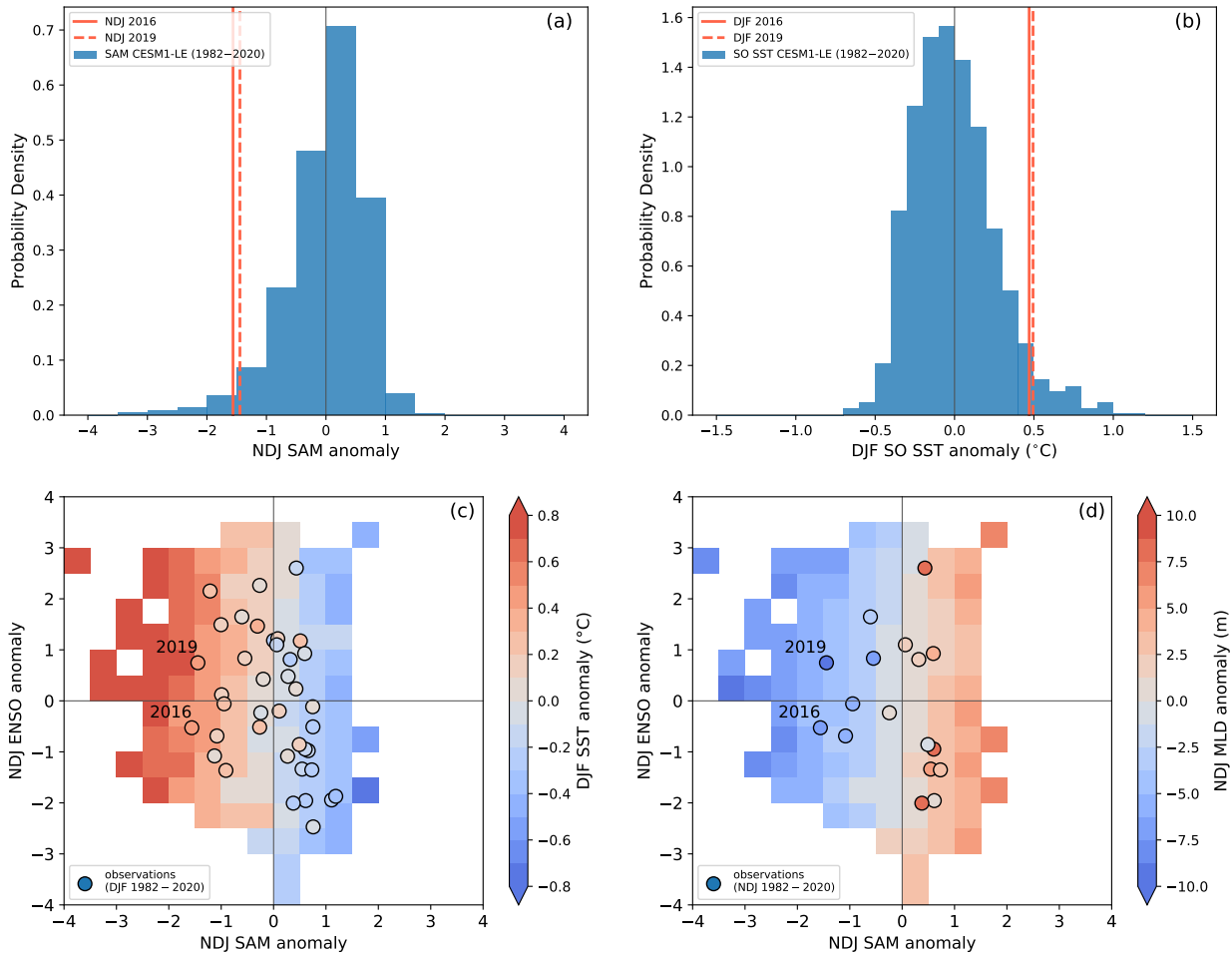
339 Additional simulations (not shown here) were conducted to evaluate the sensitivity of the mixed  
340 layer responses to the duration and sign of the wind perturbation. Prolonging the weakening of the  
341 winds leads to equivalent changes in the MLD and heating tendency anomalies, with the extended  
342 accumulation of  $\dot{T}$  anomalies resulting in a larger absolute change in MLT. Applying a positive  
343 wind perturbation produces a response opposite to the case with weaker winds, albeit with more  
344 minor MLT anomalies due to the deeper mixed layers.

345 Though idealized, these numerical simulations demonstrate that a reduction in wind-driven  
346 mixing can generate MLT anomalies similar in magnitude to those observed during the austral  
347 spring and summer of 2016/2017 and 2019/2020. The decrease in northward Ekman transport, a  
348 process not included in our idealized model, would further augment the surface warming response.

#### 357 *e. Role of internal climate variability*

358 Given the rarity of these abrupt circumpolar warming events and our short observational record,  
359 we examine output from the 40-member CESM1-LE to gain a more robust understanding of  
360 these phenomena. Specifically, we investigate the response of summertime Southern Ocean SST  
361 (December–February; DJF) to variations of SAM in the preceding austral spring. An observational  
362 analysis of the lead-lag relationship between the SAM index and DJF SST across 50°–65°S shows  
363 that maximal correlation ( $r \approx -0.75$ ) is attained when SST is lagged by one month. Therefore,  
364 we assess the relationship between Southern Ocean SST anomalies in DJF with SAM variability  
365 in November–January (NDJ) in the CESM1-LE. To isolate the effect of internal variability, we  
366 evaluate the variance of SAM and Southern Ocean SST after removing the ensemble-mean values,  
367 which represent the responses to anthropogenic forcing.

368 Though rare, abrupt Southern Ocean warming events like those observed in late 2016 and 2019  
369 appear in the CESM1-LE (Figure 7a,b). In the CESM1-LE, NDJ periods where the SAM index  
370 is more than 1.5 standard deviations below average occur roughly once every 20 years. The



349 FIG. 7. Comparisons of SAM and Southern Ocean SST variability in the 40-member CESM1-LE with  
 350 observations during 1982–2020. (a) Probability density distribution of the November–January (NDJ) SAM  
 351 index in the CESM1-LE. (b) As in (a), but for domain-averaged DJF Southern Ocean SST anomalies across  
 352 50°–65°S. (c) Composites of domain-averaged DJF Southern Ocean SST anomalies in relation to NDJ SAM and  
 353 ENSO. (d) As in (c), but showing NDJ Southern MLD anomalies. For the CESM1-LE results, anomalies refer  
 354 to deviations from the ensemble mean. In (a) and (b), the frequency distributions of SAM and Southern Ocean  
 355 SST are generated using 0.5 standard deviations and 0.1°C bins, respectively. For the observed seasonal averages  
 356 shown here, the listed year represents the year the season begins.

371 distribution of NDJ SAM events also has a notable skew towards negative SAM events (Figure 7a).  
 372 Importantly, the simulated Southern Ocean SST and MLD responses to late-spring SAM variability  
 373 are consistent with observations. In particular, the anomalous mixed layer warming and shoaling

374 observed in late 2016 and 2019 are similar in magnitude to those produced by comparable SAM  
375 events in the CESM1-LE (Figure 7c,d).

376 In the observational record, strong SAM and ENSO events sometimes co-occur (e.g., during  
377 the austral spring of 1982 and 2002; Figure 2), which makes it difficult to separate their effects.  
378 To quantify the relative effect of SAM and ENSO in the CESM1-LE, we create composites of  
379 Southern Ocean SST and MLD anomalies using 0.5 standard deviation bins. In the CESM1-LE,  
380 strong SAM and ENSO events can occur independently. While ENSO affects Southern Ocean  
381 SST via atmospheric teleconnections, this signal is communicated on sub-seasonal timescales  
382 (Li et al. 2021). In the CESM1-LE, SAM has the dominant control over domain-averaged SST  
383 and MLD anomalies across 50°S–65°S during austral spring and summer. The sensitivity of  
384 summertime Southern Ocean SST and MLD to SAM variability is less apparent for individual  
385 ensemble members, and a robust dependence on SAM only emerges after averaging anomalies  
386 across the 40-member ensemble. These results indicate that other modes of variability significantly  
387 impact interannual variations of Southern Ocean SST and MLD in austral spring.

#### 388 **4. Discussion**

389 This study demonstrates that the seasonal phasing of MLD shoaling and air-sea heat fluxes is  
390 a key driver of interannual variability in summertime Southern Ocean SST. Between September  
391 and December, the zonally averaged MLD between 50°S–65°S shoals from its winter maximum  
392 of ~150 m to its summer minimum of ~50 m (Fig. 5). The rate at which this shoaling occurs  
393 varies substantially from year to year and produces an equivalently large spread in the rate at which  
394 the mixed layer warms. In the austral spring of 2016 and 2019, the Southern Ocean mixed layer  
395 shoaled at the fastest rates observed during the Argo era, which amplified the warming effect of  
396 solar insolation when it was near its seasonal maximum. During both events, the anomalous MLD  
397 shoaling was initiated by a dramatic weakening of the circumpolar westerlies associated with strong  
398 negative SAM events. The weaker westerlies also reduced northward Ekman transport, further  
399 amplifying the mixed layer warming.

400 While several studies have shown that SAM has substantial control over springtime MLD and  
401 MLT (e.g., Sen Gupta and England 2006; Sallée et al. 2010), this study emphasizes the importance  
402 of the rate at which the mixed layer shoals in the spring and quantifies the high degree to which

403 mixed layer warming is sensitive to the timing of the SAM anomalies. In particular, a sustained  
404 negative SAM event in November is expected to yield surface warming anomalies that are at least  
405 twice that produced by a similar SAM event occurring one month earlier. The late 2016 and 2019  
406 warming events followed intense periods of negative SAM, which peaked during November and  
407 December, during which the MLT response to surface wind variability is maximal. This temporal  
408 sensitivity may explain why the negative SAM event in late 2002 did not lead to anomalous surface  
409 warming as severe as what was observed in late 2016 and 2019 (Figs. 1a, 2c). Though the late 2002  
410 negative SAM event was just as intense and more prolonged than the 2016 and 2019 SAM events,  
411 the former peaked in October before transitioning to a more neutral state in November. Conversely,  
412 the timing of the negative SAM events in late 1982 may explain the exceptionally strong warming  
413 observed that spring (Figures 1a, 2c).

414 Abrupt circumpolar surface warming events, such as those observed across the Southern Ocean  
415 in late 2016 and 2019, occur in the CESM1-LE. These events are relatively rare, occurring roughly  
416 every 20 years in the CESM1-LE. Additionally, the Southern Ocean SST and MLD response  
417 to SAM in the CESM1-LE aligns well with recent observations. The CESM1-LE also features  
418 springtime negative SAM events that are more extreme than what has been observed over the past  
419 four decades, which suggests that the SAM variability may drive even more intense summertime  
420 surface warming anomalies in the future. In the CESM1-LE, SAM has a much stronger influence on  
421 zonally averaged summertime SST variability across the circumpolar channel than ENSO. However,  
422 examining individual ensemble members reveals that ENSO and other modes of variability can  
423 substantially modulate summertime Southern Ocean SST variability in a given year. Nevertheless,  
424 we conclude that the anomalous circumpolar warming of late 2016 and 2019 were primarily  
425 manifestations of internal climate variability. This assessment is in agreement with previous  
426 analyses that examine mechanisms responsible for recent declines in Antarctic SIE (e.g., Stuecker  
427 et al. 2017; Eayrs et al. 2021).

428 As the circumpolar westerlies continue to intensify and shift poleward, the upper overturning cell  
429 of the Southern Ocean is expected to strengthen, increasing the upwelling of warm Circumpolar  
430 Deep Water across the Antarctic sea ice zone (Ferreira et al. 2015; Kostov et al. 2017). Additionally,  
431 stronger winds will likely energize eddies across the circumpolar channel that will partially negate  
432 the Ekman overturning response (Farneti et al. 2010; Doddridge et al. 2019). Warming associated

433 with these overturning adjustments may be significant if, as expected, they persist over interannual  
434 to decadal timescales. There is evidence that upper ocean upwelling trends contributed to the  
435 prolonged period of below-average Antarctic SIE between 2016 and 2020 (Meehl et al. 2019). The  
436 recent decline in Antarctic sea ice cover has been most pronounced in the Weddell Sea (Parkinson  
437 2019), which featured large open-ocean polynyas and deep convection during the winters of 2016  
438 and 2017 (Cheon and Gordon 2019). These polynya events were facilitated by enhanced upwelling  
439 across the Weddell Gyre, which gradually eroded the local pycnocline and preconditioned the  
440 region for deep convection (Campbell et al. 2019). Thus, we surmise that the anomalous Southern  
441 Ocean surface warming and sea ice loss since 2016 were primarily due to a culmination of several  
442 climate processes acting over sub-seasonal to interannual timescales.

443 Additional work is needed to determine how the variability of SAM and its impacts on Southern  
444 Ocean MLD and SST will evolve under anthropogenic forcing. Previous studies have primarily  
445 focused on the mean-state ocean response to the ongoing trend toward a more positive SAM phase, in  
446 particular, the ocean overturning response to a strengthening and poleward shift of the circumpolar  
447 westerlies (e.g., Bitz and Polvani 2012; Ferreira et al. 2015; Kostov et al. 2017). However, our  
448 results demonstrate that near-surface processes acting on sub-seasonal timescales will play a key  
449 role in setting future surface warming extremes. While the current positive trend in the SAM index  
450 favors more vigorous wind-driven mixing and deeper mixed layers, concurrent surface warming  
451 and freshening trends favor stronger near-surface stratification and possibly shallower mixed layers  
452 (Panassa et al. 2018). These competing processes have deepened the Southern Ocean mixed layer  
453 and strengthening the upper ocean stratification (Sallée et al. 2021). The extent to which these  
454 trends persist will impact the frequency and intensity of future abrupt surface warming events and  
455 marine heatwaves in the Southern Ocean.

456 The evolving seasonality of SAM will likely impact the occurrence of extreme warming events  
457 in the Southern Ocean. Recent SAM trends have been attributed to stratospheric ozone depletion,  
458 which favors a strengthening and poleward shift of circumpolar westerlies during austral summer  
459 (Thompson and Solomon 2002; Polvani et al. 2011). As the stratospheric ozone levels recover, these  
460 seasonal SAM trends will subside and possibly reverse (Solomon et al. 2016; Banerjee et al. 2020).  
461 Separately, the increase in greenhouse-gas concentrations will contribute to a strengthening of the  
462 circumpolar westerlies; the extent to which this effect will negate the ozone-induced SAM trends

463 is unclear. Nevertheless, if the Antarctic ozone hole recovery continues, the ensuing reduction in  
464 positive SAM anomalies in austral summer will favor more extreme surface warming events during  
465 these months.

## 466 **5. Conclusions**

467 The abrupt Southern Ocean surface warming events of late 2016 and 2019 were primarily  
468 caused by amplified air-sea heating and reduced northward Ekman transport. The former effect  
469 was dominant and was caused by an unusually early springtime shoaling of the Southern Ocean  
470 mixed layer. Both surface warming events were initiated by a collapse of the circumpolar westerlies  
471 associated with extreme negative SAM events. Equivalent warming events are found in the CESM1-  
472 LE, wherein the Southern Ocean SST and MLD response to SAM are consistent with recent  
473 observations. Therefore, it is plausible that recent Southern Ocean surface warming anomalies  
474 were largely the result of internal variability. A key insight from this analysis is that the Southern  
475 Ocean SST response is highly sensitive to the timing SAM anomalies, with negative SAM anomalies  
476 in late spring providing the strongest surface warming. By examining the upper ocean processes  
477 that can produce extreme circumpolar summertime warming, we have shed light on the processes  
478 that help establish the upper bound of surface temperatures that may occur in the Southern Ocean.

479 This work mainly elucidates mechanisms that can lead to extreme circumpolar summertime  
480 warming across the Southern ocean. Additional processes operating on smaller spatial scales, such  
481 as mesoscale and submesoscale processes (Gao et al. 2022; du Plessis et al. 2022), may augment  
482 large-scale warming patterns and create more severe local SST extremes. Moreover, the mixed  
483 layer response to SAM has strong inter-basin asymmetries, featuring a prominent dipole MLT  
484 anomaly across the eastern Pacific and western Atlantic (Sen Gupta and England 2006; Sallée et al.  
485 2010). Though these smaller-scale processes and features are critically important for understanding  
486 regional warming patterns, we emphasize that the warming mechanisms we explore in this study,  
487 specifically the MLD response to wind perturbations in austral spring, operate across all spatial  
488 scales and will contribute to local warming patterns. Further work is also needed to examine  
489 how these abrupt summertime warming events may impact upper ocean process in subsequent  
490 seasons. Previous work has shown that strong summertime winds may reduce Antarctic SIE the  
491 following winter, whereby enhanced wind-driven mixing in the summer causes an increase in

492 ocean heat uptake that is released during the fall (Doddridge et al. 2021). Therefore, it is plausible  
493 that anomalously weak summertime winds could impact subsequent sea ice growth via a similar  
494 mechanism.

495 As the Southern Ocean climate evolves over the 21st century, the frequency and intensity of  
496 surface warming extremes will depend on the evolution of SAM, surface winds, and MLD. Though  
497 past studies have shown the current trend towards positive SAM will eventually lead to sustained  
498 surface warming across the Southern Ocean (Ferreira et al. 2015; Bitz and Polvani 2012), it is  
499 less clear how the interannual variability of SAM and summertime Southern Ocean SST will  
500 co-evolve. The severity of future surface warming events in the Southern Ocean will partly depend  
501 on the evolution of the regional MLD; if the springtime MLD shoals over the next century, this  
502 will favor more intense summertime warming events. Projecting the evolution of Southern Ocean  
503 MLD is complicated by its dependence on competing processes: the projected strengthening of  
504 the circumpolar westerlies and increases in surface buoyancy fluxes via warming and enhanced  
505 freshwater fluxes (Meredith et al. 2019; Sallée et al. 2021). In a scenario where stronger winds  
506 dominate MLD trends, the Southern Ocean surface may experience steady decadal warming but  
507 reduced interannual variability due to a concurrent deepening of the mixed layer in spring and  
508 summer. Alternatively, if the surface mixed layer shoals over the coming decades, the region will  
509 likely experience more intense surface warming extremes, which would exacerbate the impact  
510 of the expected time-mean surface warming trend. These extreme warming scenarios will have  
511 profound consequences for the viability of regional ecosystems and biogeochemical processes.  
512 Thus, it is critical to establish bounds on the temporal variance that may envelope future warming  
513 trends.

514 *Acknowledgments.* E.A.W. acknowledges support from Caltech’s Terrestrial Hazard Observations  
515 and Reporting Center. D.B.B. was supported by the National Science Foundation Graduate  
516 Research Fellowship Program (NSF Grant DGE-1745301). A.F.T. received support from NSF  
517 award OCE-1756956 and the Internal Research and Technology Development program (Earth  
518 2050), Jet Propulsion Laboratory, California Institute of Technology. E.A.W. and S.C.R. received  
519 support through the SOCCOM Project, funded by the National Science Foundation, Division of  
520 Polar Programs (NSF PLR-1425989 and OPP-1936222). E.A.W. and S.C.R. also received funding  
521 from NOAA as part of the US Argo Program via grant NA20OAR4320271 to the University of  
522 Washington. We thank Edward Doddridge and an anonymous referee for insightful feedback that  
523 substantially improved the quality of this manuscript.

524 *Data availability statement.* All data and reanalysis products used in this study are sourced  
525 from publicly accessible repositories. NOAA Optimum Interpolation SST V2 data were  
526 retrieved from <https://psl.noaa.gov/data/gridded/data.noaa.oisst.v2.html>. The  
527 Roemmich-Gilson Argo product was downloaded from [https://sio-argo.ucsd.edu/RG\\_](https://sio-argo.ucsd.edu/RG_Climatology.html)  
528 [Climatology.html](https://sio-argo.ucsd.edu/RG_Climatology.html). ERA5 reanalysis can be accessed at [https://doi.org/10.24381/cds.](https://doi.org/10.24381/cds.f17050d7)  
529 [f17050d7](https://doi.org/10.24381/cds.f17050d7). Model output from the CESM1-LE can be downloaded from [https://www.cesm.](https://www.cesm.ucar.edu/projects/community-projects/LENS/data-sets.html)  
530 [ucar.edu/projects/community-projects/LENS/data-sets.html](https://www.cesm.ucar.edu/projects/community-projects/LENS/data-sets.html). NOAA/NSIDC Cli-  
531 mate Data Record of Passive Microwave Sea Ice Concentration (Version 4) can be accessed at  
532 <https://doi.org/10.7265/efmz-2t65z>. Python code for carrying out analysis and generat-  
533 ing figures is available at <https://doi.org/10.5281/zenodo.6588645>.

## 534 APPENDIX

### 535 **A1. Ensemble experiments with a 1D mixing model**

536 To evaluate the impact of wind perturbations on MLT warming, we use a modified version of the  
537 Kraus-Turner 1D upper ocean mixing model (Kraus and Turner 1967; Niiler 1975; Niiler and Kraus  
538 1977). This bulk mixed layer model simulates the evolution of the surface mixed layer by balancing  
539 the stabilizing effect of surface buoyancy fluxes (i.e., the addition of heat or freshwater to the water  
540 column) and the destabilizing effect of wind-driven mixing. Variants of the Kraus-Turner model  
541 have been used extensively to study surface mixed layer variations over a wide range of settings,

542 including in subpolar regions (Biddle et al. 2017). Following Chen et al. (1994), the entrainment  
 543 rate,  $w_{ent}$ , of the mixed layer is given by

$$544 \quad w_{ent} = \frac{P_w - P_b}{h_m \Delta b}, \quad (A1)$$

545 where  $\Delta b$  is the buoyancy difference across the base of the mixed layer, and  $P_w$  and  $P_b$  are work  
 546 provided by surface wind stress and the potential energy supplied by surface buoyancy fluxes,  
 547 respectively.  $P_w$  and  $P_b$  are given by

$$548 \quad P_w = 2\gamma_1 u_*^3, \quad (A2)$$

$$549 \quad P_b = \frac{h_m}{2} [(1 + \gamma_2) B_0 - (1 - \gamma_2) |B_0|], \quad (A3)$$

551 where  $\gamma_1 = 0.4$  and  $\gamma_2 = 0.18$  are empirically derived mixing coefficients,  $u_*$  is the friction velocity,  
 552 and  $B_0$  is the total surface buoyancy flux. The above formulation is valid for a stably stratified  
 553 water column ( $\Delta b > 0$ ). For scenarios where  $P_w - P_b > 0$ , the mixed layer deepens and (A1) is  
 554 used to determine the entrainment rate. For cases of mixed layer shoaling, we assume  $P_w$  and  $P_b$   
 555 are in balance and we use the relationships (A2) and (A3) to determine  $h_m$ .

556 The mixing model is initialized with idealized temperature and salinity profiles representative  
 557 of the circumpolar channel between 50°–65°S in early October. At the start of each simulation,  
 558 the mixed layer depth is set to 125 m, and temperature and salinity in the mixed layer are set  
 559 to 1 °C and 33.4 PSU, respectively. Below the mixed layer, there is a 150 m thick seasonal  
 560 pycnocline, across which temperature and salinity linearly transition to fixed values of 0°C and  
 561 ~33.6 PSU, respectively. We prescribe a surface heat flux that approximates the climatological  
 562 net surface heating across the circumpolar channel between October and March (150 days total).  
 563 To isolate the impact of surface winds and heating, we impose a constant surface freshwater flux  
 564 (i.e., precipitation minus evaporation) of 1 mm day<sup>-1</sup>. The buoyancy forcing is combined with a  
 565 synthetically generated surface wind stress  $\tau$ , which is modeled as the sum of a red-noise sequence

566  $\hat{\tau}(t)$  and a mean offset  $\bar{\tau}$ :

$$567 \quad \tau(t) = \hat{\tau}(t) + \bar{\tau}, \quad (\text{A4})$$

$$568 \quad \hat{\tau}(t) = a \hat{\tau}(t - \Delta t) + \sqrt{(1 - a^2)} \epsilon(t), \quad (\text{A5})$$

569

570 where  $a = 0.9$  is the lag-1 auto-correlation coefficient,  $\Delta t = 6$  hours is the time step,  $\epsilon$  is a randomly  
571 generated white noise sequence with a standard deviation of 0.05, and  $\bar{\tau} = 0.1 \text{ N m}^{-2}$ . The  
572 numerical model is evolved with a vertical resolution of 0.25 m and a 6 hourly time step. A total of  
573 six ensemble experiments are carried out: one control experiment consisting of 200 independent  
574 simulations, each with a unique wind forcing, and five perturbation experiments wherein  $\bar{\tau}$  is  
575 reduced over different time windows, centered on days 15, 45, 75, 105, and 135 days (after October  
576 1). For the perturbation experiments, the magnitude of the time-mean wind stress is reduced by a  
577 maximum of 50% using a Gaussian window with a standard deviation of 5 days. By perturbing  $\bar{\tau}$   
578 in Equation (A5), the temporal variance of  $\tau$  is preserved.

## 579 **References**

- 580 Armour, K. C., J. Marshall, J. R. Scott, A. Donohoe, and E. R. Newsom, 2016: Southern Ocean  
581 warming delayed by circumpolar upwelling and equatorward transport. *Nature Geoscience*, **9** (7),  
582 549–554, <https://doi.org/10.1038/ngeo2731>.
- 583 Banerjee, A., J. C. Fyfe, L. M. Polvani, D. Waugh, and K.-L. Chang, 2020: A pause in Southern  
584 Hemisphere circulation trends due to the Montreal Protocol. *Nature*, **579** (7800), 544–548,  
585 <https://doi.org/10.1038/s41586-020-2120-4>.
- 586 Biddle, L. C., K. J. Heywood, J. Kaiser, and A. Jenkins, 2017: Glacial meltwater identification  
587 in the Amundsen Sea. *Journal of Physical Oceanography*, JPO–D–16–0221.1, <https://doi.org/10.1175/JPO-D-16-0221.1>.
- 589 Bintanja, R., G. J. V. Oldenborgh, S. S. Drijfhout, B. Wouters, and C. A. Katsman, 2013: Important  
590 role for ocean warming and increased ice-shelf melt in Antarctic sea-ice expansion. *Nature*  
591 *Geoscience*, **6** (5), 376–379, <https://doi.org/10.1038/ngeo1767>.

592 Bitz, C. M., and L. M. Polvani, 2012: Antarctic climate response to stratospheric ozone depletion  
593 in a fine resolution ocean climate model. *Geophysical Research Letters*, **39** (20), [https://doi.org/](https://doi.org/10.1029/2012GL053393)  
594 10.1029/2012GL053393.

595 Campbell, E. C., E. A. Wilson, G. W. Moore, S. C. Riser, C. E. Brayton, M. R. Mazloff, and L. D.  
596 Talley, 2019: Antarctic offshore polynyas linked to Southern Hemisphere climate anomalies.  
597 *Nature*, **570** (7761), 319–325, <https://doi.org/10.1038/s41586-019-1294-0>.

598 Carranza, M. M., and S. T. Gille, 2015: Southern Ocean wind-driven entrainment enhances  
599 satellite chlorophyll-a through the summer. *Journal of Geophysical Research: Oceans*, **120** (1),  
600 304–323, <https://doi.org/10.1002/2014JC010203>.

601 Cavalieri, D. J., C. L. Parkinson, and K. Y. Vinnikov, 2003: 30-year satellite record reveals  
602 contrasting Arctic and Antarctic decadal sea ice variability. *Geophysical Research Letters*,  
603 **30** (18), <https://doi.org/10.1029/2003GL018031>.

604 Chen, D., L. M. Rothstein, and A. J. Busalacchi, 1994: A Hybrid Vertical Mixing Scheme and Its  
605 Application to Tropical Ocean Models. *Journal of Physical Oceanography*, **24** (10), 2156–2179,  
606 [https://doi.org/10.1175/1520-0485\(1994\)024<2156:AHVMSA>2.0.CO;2](https://doi.org/10.1175/1520-0485(1994)024<2156:AHVMSA>2.0.CO;2).

607 Cheon, W. G., and A. L. Gordon, 2019: Open-ocean polynyas and deep convection in the Southern  
608 Ocean. *Scientific Reports*, **9** (1), 6935, <https://doi.org/10.1038/s41598-019-43466-2>.

609 Chung, E.-S., and Coauthors, 2022: Antarctic sea-ice expansion and Southern Ocean cooling linked  
610 to tropical variability. *Nature Climate Change*, <https://doi.org/10.1038/s41558-022-01339-z>.

611 Ciasto, L. M., and M. H. England, 2011: Observed ENSO teleconnections to Southern Ocean SST  
612 anomalies diagnosed from a surface mixed layer heat budget. *Geophysical Research Letters*,  
613 **38** (9), <https://doi.org/10.1029/2011GL046895>.

614 Danabasoglu, G., S. C. Bates, B. P. Briegleb, S. R. Jayne, M. Jochum, W. G. Large, S. Peacock, and  
615 S. G. Yeager, 2012: The CCSM4 Ocean Component. *Journal of Climate*, **25** (5), 1361–1389,  
616 <https://doi.org/10.1175/JCLI-D-11-00091.1>.

617 de Boyer Montégut, C., G. Madec, A. S. Fischer, A. Lazar, and D. Iudicone, 2004: Mixed layer depth  
618 over the global ocean: An examination of profile data and a profile-based climatology. *Journal*  
619 *of Geophysical Research C: Oceans*, **109** (12), 1–20, <https://doi.org/10.1029/2004JC002378>.

- 620 Ding, Q., E. J. Steig, D. S. Battisti, and J. M. Wallace, 2012: Influence of the tropics  
621 on the southern annular mode. *Journal of Climate*, **25** (18), 6330–6348, [https://doi.org/](https://doi.org/10.1175/JCLI-D-11-00523.1)  
622 10.1175/JCLI-D-11-00523.1.
- 623 Doddridge, E. W., and J. Marshall, 2017: Modulation of the Seasonal Cycle of Antarctic Sea  
624 Ice Extent Related to the Southern Annular Mode. *Geophysical Research Letters*, **44** (19),  
625 9761–9768, <https://doi.org/10.1002/2017GL074319>.
- 626 Doddridge, E. W., J. Marshall, H. Song, J.-M. Campin, and M. Kelley, 2021: Southern Ocean Heat  
627 Storage, Reemergence, and Winter Sea Ice Decline Induced by Summertime Winds. *Journal of*  
628 *Climate*, **34** (4), 1403–1415, <https://doi.org/10.1175/JCLI-D-20-0322.1>.
- 629 Doddridge, E. W., J. Marshall, H. Song, J. M. Campin, M. Kelley, and L. Nazarenko,  
630 2019: Eddy Compensation Dampens Southern Ocean Sea Surface Temperature Response  
631 to Westerly Wind Trends. *Geophysical Research Letters*, **46** (8), 4365–4377, [https://doi.org/](https://doi.org/10.1029/2019GL082758)  
632 10.1029/2019GL082758.
- 633 Dong, S., S. T. Gille, and J. Sprintall, 2007: An assessment of the Southern Ocean mixed layer  
634 heat budget. *Journal of Climate*, **20** (17), 4425–4442, <https://doi.org/10.1175/JCLI4259.1>.
- 635 Dong, S., J. Sprintall, S. T. Gille, and L. Talley, 2008: Southern ocean mixed-layer depth from  
636 Argo float profiles. *Journal of Geophysical Research: Oceans*, **113** (6), [https://doi.org/10.1029/](https://doi.org/10.1029/2006JC004051)  
637 2006JC004051.
- 638 du Plessis, M. D., S. Swart, L. C. Biddle, I. S. Giddy, P. M. S. Monteiro, C. J. C. Reason,  
639 A. F. Thompson, and S. Nicholson, 2022: The Daily-Resolved Southern Ocean Mixed Layer:  
640 Regional Contrasts Assessed Using Glider Observations. *Journal of Geophysical Research:*  
641 *Oceans*, **127** (4), <https://doi.org/10.1029/2021JC017760>, URL [https://onlinelibrary.wiley.com/](https://onlinelibrary.wiley.com/doi/10.1029/2021JC017760)  
642 [doi/10.1029/2021JC017760](https://doi.org/10.1029/2021JC017760).
- 643 Eayrs, C., X. Li, M. N. Raphael, and D. M. Holland, 2021: Rapid decline in Antarctic sea ice  
644 in recent years hints at future change. *Nature Geoscience*, **14** (7), 460–464, [https://doi.org/](https://doi.org/10.1038/s41561-021-00768-3)  
645 10.1038/s41561-021-00768-3.

- 646 Fan, T., C. Deser, and D. P. Schneider, 2014: Recent Antarctic sea ice trends in the context of  
647 Southern Ocean surface climate variations since 1950. *Geophysical Research Letters*, **41** (7),  
648 2419–2426, <https://doi.org/10.1002/2014GL059239>.
- 649 Farneti, R., T. L. Delworth, A. J. Rosati, S. M. Griffies, and F. Zeng, 2010: The role of mesoscale  
650 eddies in the rectification of the Southern ocean response to climate change. *Journal of Physical  
651 Oceanography*, **40** (7), 1539–1557, <https://doi.org/10.1175/2010JPO4353.1>.
- 652 Ferreira, D., J. Marshall, C. M. Bitz, S. Solomon, and A. Plumb, 2015: Antarctic ocean and sea ice  
653 response to ozone depletion: A two-time-scale problem. *Journal of Climate*, **28** (3), 1206–1226,  
654 <https://doi.org/10.1175/JCLI-D-14-00313.1>.
- 655 Fox-Kemper, B., R. Ferrari, and R. Hallberg, 2008: Parameterization of Mixed Layer Eddies. Part  
656 I: Theory and Diagnosis. *Journal of Physical Oceanography*, **38** (6), 1145–1165, [https://doi.org/  
657 10.1175/2007JPO3792.1](https://doi.org/10.1175/2007JPO3792.1).
- 658 Frölicher, T. L., E. M. Fischer, and N. Gruber, 2018: Marine heatwaves under global warming.  
659 *Nature*, **560** (7718), 360–364, <https://doi.org/10.1038/s41586-018-0383-9>.
- 660 Gao, Y., I. Kamenkovich, N. Perlin, and B. Kirtman, 2022: Oceanic Advection Controls Mesoscale  
661 Mixed Layer Heat Budget and Air–Sea Heat Exchange in the Southern Ocean. *Journal of Physical  
662 Oceanography*, **52** (4), 537–555, <https://doi.org/10.1175/JPO-D-21-0063.1>.
- 663 Haumann, F. A., N. Gruber, and M. Münnich, 2020: Sea-Ice Induced Southern Ocean Subsurface  
664 Warming and Surface Cooling in a Warming Climate. *AGU Advances*, **1** (2), [https://doi.org/  
665 10.1029/2019AV000132](https://doi.org/10.1029/2019AV000132).
- 666 Hersbach, H., and Coauthors, 2020: The ERA5 global reanalysis. *Quarterly Journal of the Royal  
667 Meteorological Society*, **146** (730), 1999–2049, <https://doi.org/10.1002/qj.3803>.
- 668 Hobday, A. J., and Coauthors, 2016: A hierarchical approach to defining marine heatwaves.  
669 *Progress in Oceanography*, **141**, 227–238, <https://doi.org/10.1016/j.pocean.2015.12.014>.
- 670 Holbrook, N. J., and Coauthors, 2019: A global assessment of marine heatwaves and their drivers.  
671 *Nature Communications*, **10** (1), 2624, <https://doi.org/10.1038/s41467-019-10206-z>.

- 672 Kay, J. E., and Coauthors, 2015: The Community Earth System Model (CESM) Large Ensem-  
673 ble Project: A Community Resource for Studying Climate Change in the Presence of Inter-  
674 nal Climate Variability. *Bulletin of the American Meteorological Society*, **96 (8)**, 1333–1349,  
675 <https://doi.org/10.1175/BAMS-D-13-00255.1>.
- 676 Kostov, Y., J. Marshall, U. Hausmann, K. C. Armour, D. Ferreira, and M. M. Holland, 2017:  
677 Fast and slow responses of Southern Ocean sea surface temperature to SAM in coupled climate  
678 models. *Climate Dynamics*, **48 (5-6)**, 1595–1609, <https://doi.org/10.1007/s00382-016-3162-z>.
- 679 Kraus, E. B., and J. S. Turner, 1967: A one-dimensional model of the seasonal thermocline II.  
680 The general theory and its consequences. *Tellus*, **19 (1)**, 98–106, <https://doi.org/10.3402/tellusa.v19i1.9753>.
- 682 Li, X., and Coauthors, 2021: Tropical teleconnection impacts on Antarctic climate changes. *Nature*  
683 *Reviews Earth & Environment*, **2 (10)**, 680–698, <https://doi.org/10.1038/s43017-021-00204-5>.
- 684 Marshall, G. J., 2003: Trends in the Southern Annular Mode from observations and reanalyses.  
685 *Journal of Climate*, **16 (24)**, 4134–4143, [https://doi.org/10.1175/1520-0442\(2003\)016<4134:  
686 TITSAM>2.0.CO;2](https://doi.org/10.1175/1520-0442(2003)016<4134:TITSAM>2.0.CO;2).
- 687 Meehl, G. A., J. M. Arblaster, C. M. Bitz, C. T. Y. Chung, and H. Teng, 2016: Antarctic sea-ice  
688 expansion between 2000 and 2014 driven by tropical Pacific decadal climate variability. *Nature*  
689 *Geoscience*, **9 (8)**, 590–595, <https://doi.org/10.1038/ngeo2751>.
- 690 Meehl, G. A., J. M. Arblaster, C. T. Y. Chung, M. M. Holland, A. DuVivier, L. A.  
691 Thompson, D. Yang, and C. M. Bitz, 2019: Sustained ocean changes contributed to sud-  
692 den Antarctic sea ice retreat in late 2016. *Nature Communications*, **10 (1)**, [https://doi.org/  
693 10.1038/s41467-018-07865-9](https://doi.org/10.1038/s41467-018-07865-9).
- 694 Meier, W., F. Fetterer, M. Savoie, S. Mallory, R. Duerr, and J. Stroeve, 2013: NOAA/NSIDC  
695 Climate Data Record of Passive Microwave Sea Ice Concentration. NSIDC: National Snow and  
696 Ice Data Center, <https://doi.org/10.7265/N59P2ZTG>.
- 697 Meredith, M., and Coauthors, 2019: Polar Regions. *Ocean Cryosph. a Chang. Clim.*, H.-O. Pörtner,  
698 D. C. Roberts, V. Masson-Delmotte, P. Zhai, M. Tignor, E. Poloczanska, K. Mintenbeck,

699 A. Alegría, M. Nicolai, A. Okem, J. Petzold, B. Rama, and N. M. Weyer, Eds., Cambridge  
700 University Press, Cambridge, chap. 3, 203–320, <https://doi.org/10.1017/9781009157964.005>.

701 Niiler, P. P., 1975: The deepening of the wind-mixed layer. *Journal of Marine Research*, **33** (3),  
702 405–422.

703 Niiler, P. P., and E. B. Kraus, 1977: One Dimensional Models of the Upper Ocean. Pergamon,  
704 143–172 pp.

705 Oliver, E. C. J., J. A. Benthuisen, S. Darmaraki, M. G. Donat, A. J. Hobday, N. J. Holbrook, R. W.  
706 Schlegel, and A. S. Gupta, 2021: Marine Heatwaves. *Annual Review of Marine Science*, **13** (1),  
707 313–342, <https://doi.org/10.1146/annurev-marine-032720-095144>.

708 Panassa, E., C. Völker, D. Wolf-Gladrow, and J. Hauck, 2018: Drivers of Interannual Variability  
709 of Summer Mixed Layer Depth in the Southern Ocean Between 2002 and 2011. *Journal of*  
710 *Geophysical Research: Oceans*, **123** (8), 5077–5090, <https://doi.org/10.1029/2018JC013901>.

711 Parkinson, C. L., 2019: A 40-y record reveals gradual Antarctic sea ice increases followed by  
712 decreases at rates far exceeding the rates seen in the Arctic. *Proceedings of the National Academy*  
713 *of Sciences*, **116** (29), 14 414–14 423, <https://doi.org/10.1073/pnas.1906556116>.

714 Pellichero, V., J. B. Sallée, S. Schmidtko, F. Roquet, and J. B. Charrassin, 2017: The ocean  
715 mixed layer under Southern Ocean sea-ice: Seasonal cycle and forcing. *Journal of Geophysical*  
716 *Research: Oceans*, **122** (2), 1608–1633, <https://doi.org/10.1002/2016JC011970>.

717 Polvani, L. M., D. W. Waugh, G. J. P. Correa, and S. W. Son, 2011: Stratospheric ozone de-  
718 pletion: The main driver of twentieth-century atmospheric circulation changes in the Southern  
719 Hemisphere. *Journal of Climate*, **24** (3), 795–812, <https://doi.org/10.1175/2010JCLI3772.1>.

720 Purich, A., and M. H. England, 2019: Tropical Teleconnections to Antarctic Sea Ice During Austral  
721 Spring 2016 in Coupled Pacemaker Experiments. *Geophysical Research Letters*, **46** (12), 6848–  
722 6858, <https://doi.org/10.1029/2019GL082671>.

723 Purich, A., M. H. England, W. Cai, A. Sullivan, and P. J. Durack, 2018: Impacts of broad-scale  
724 surface freshening of the Southern Ocean in a coupled climate model. *Journal of Climate*, **31** (7),  
725 2613–2632, <https://doi.org/10.1175/JCLI-D-17-0092.1>.

- 726 Rackow, T., S. Danilov, H. F. Goessling, H. H. Hellmer, D. V. Sein, T. Semmler, D. Sidorenko, and  
727 T. Jung, 2022: Delayed Antarctic sea-ice decline in high-resolution climate change simulations.  
728 *Nature Communications*, **13** (1), 637, <https://doi.org/10.1038/s41467-022-28259-y>.
- 729 Reynolds, R. W., N. A. Rayner, T. M. Smith, D. C. Stokes, and W. Wang, 2002: An improved in situ  
730 and satellite SST analysis for climate. *Journal of Climate*, **15** (13), 1609–1625, [https://doi.org/10.1175/1520-0442\(2002\)015<1609:AIISAS>2.0.CO;2](https://doi.org/10.1175/1520-0442(2002)015<1609:AIISAS>2.0.CO;2).
- 732 Roemmich, D., and J. Gilson, 2009: The 2004-2008 mean and annual cycle of temperature, salinity,  
733 and steric height in the global ocean from the Argo Program. *Progress in Oceanography*, **82** (2),  
734 81–100, <https://doi.org/10.1016/j.pocean.2009.03.004>.
- 735 Sallée, J. B., K. G. Speer, and S. R. Rintoul, 2010: Zonally asymmetric response of the Southern  
736 Ocean mixed-layer depth to the Southern Annular Mode. *Nature Geoscience*, **3** (4), 273–279,  
737 <https://doi.org/10.1038/ngeo812>.
- 738 Sallée, J.-B., and Coauthors, 2021: Summertime increases in upper-ocean stratification and mixed-  
739 layer depth. *Nature*, **591** (7851), 592–598, <https://doi.org/10.1038/s41586-021-03303-x>.
- 740 Schlosser, E., F. A. Haumann, and M. N. Raphael, 2018: Atmospheric influences on the  
741 anomalous 2016 Antarctic sea ice decay. *Cryosphere*, **12** (3), 1103–1119, <https://doi.org/10.5194/tc-12-1103-2018>.
- 743 Sen Gupta, A., and M. H. England, 2006: Coupled ocean-atmosphere-ice response to variations  
744 in the southern annular mode. *Journal of Climate*, **19** (18), 4457–4486, <https://doi.org/10.1175/JCLI3843.1>.
- 746 Simmonds, I., 2015: Comparing and contrasting the behaviour of Arctic and Antarctic sea ice  
747 over the 35 year period 1979-2013. *Annals of Glaciology*, **56** (69), 18–28, <https://doi.org/10.3189/2015AoG69A909>.
- 749 Smale, D. A., and Coauthors, 2019: Marine heatwaves threaten global biodiversity and the  
750 provision of ecosystem services. *Nature Climate Change*, **9** (4), 306–312, <https://doi.org/10.1038/s41558-019-0412-1>.
- 751

- 752 Solomon, S., D. J. Ivy, D. Kinnison, M. J. Mills, R. R. Neely, and A. Schmidt, 2016: Emergence  
753 of healing in the Antarctic ozone layer. *Science*, **353 (6296)**, 269–274, [https://doi.org/10.1126/](https://doi.org/10.1126/science.aae0061)  
754 [science.aae0061](https://doi.org/10.1126/science.aae0061).
- 755 Stuecker, M. F., C. M. Bitz, and K. C. Armour, 2017: Conditions leading to the unprecedented low  
756 Antarctic sea ice extent during the 2016 austral spring season. *Geophysical Research Letters*,  
757 **44 (17)**, 9008–9019, <https://doi.org/10.1002/2017GL074691>.
- 758 Tamsitt, V., L. D. Talley, M. R. Mazloff, and I. Cerovecki, 2016: Zonal variations in  
759 the Southern Ocean heat budget. *Journal of Climate*, **29 (18)**, 6563–6579, [https://doi.org/](https://doi.org/10.1175/JCLI-D-15-0630.1)  
760 [10.1175/JCLI-D-15-0630.1](https://doi.org/10.1175/JCLI-D-15-0630.1).
- 761 Thompson, D. W. J., and S. Solomon, 2002: Interpretation of Recent Southern Hemisphere Climate  
762 Change. *Science*, **296 (5569)**, 895–899, <https://doi.org/10.1126/science.1069270>.
- 763 Turner, J., T. Phillips, G. J. Marshall, J. S. Hosking, J. O. Pope, T. J. Bracegirdle, and P. Deb, 2017:  
764 Unprecedented springtime retreat of Antarctic sea ice in 2016. *Geophysical Research Letters*,  
765 **44 (13)**, 6868–6875, <https://doi.org/10.1002/2017GL073656>.
- 766 Wang, G., H. H. Hendon, J. M. Arblaster, E. P. Lim, S. Abhik, and P. van Rensch, 2019: Com-  
767 pounding tropical and stratospheric forcing of the record low Antarctic sea-ice in 2016. *Nature*  
768 *Communications*, **10 (1)**, 13, <https://doi.org/10.1038/s41467-018-07689-7>.
- 769 Yuan, X., and D. G. Martinson, 2000: Antarctic sea ice extent variability and its global connectivity.  
770 *Journal of Climate*, **13 (10)**, 1697–1717, [https://doi.org/10.1175/1520-0442\(2000\)013<1697:](https://doi.org/10.1175/1520-0442(2000)013<1697:ASIEVA>2.0.CO;2)  
771 [ASIEVA>2.0.CO;2](https://doi.org/10.1175/1520-0442(2000)013<1697:ASIEVA>2.0.CO;2).
- 772 Zhang, L., T. L. Delworth, W. Cooke, and X. Yang, 2019: Natural variability of Southern  
773 Ocean convection as a driver of observed climate trends. *Nature Climate Change*, **9 (1)**, 59–65,  
774 <https://doi.org/10.1038/s41558-018-0350-3>.